journal homepage: www.brodogradnja.fsb.hr

Brodogradnja

An International Journal of Naval Architecture and Ocean Engineering for Research and Development

Numerical study of the influence of hydrofoil hydrodynamic performance considering near-free surface

Yuanhui Wei[1], *Jianing Zhang*[1*], *Kaihao Liu*[1], *Jiazhen Pan*[1], *Lei Zhang*[1], *Weimin Chen*[2], *Qingshan Zhang*[2]

[1] *School of Naval Architecture and Ocean Engineering, Dalian Maritime University, Dalian, 116026, China*

[2] *State Key Laboratory of Maritime Technology and Safety, Shanghai Ship and Shipping Research Institute Co., Ltd, Shanghai, 200135, China*

ARTICLE INFO

Keywords:
Bionic hydrofoil
Flapping wing
Overset mesh
Adaptive mesh
CFD
Near-free Surface

ABSTRACT

Bionic flapping hydrofoil motion is increasingly used in bionic underwater robots. However, many scholars have focused their attention on the navigation problem in deep-water environments, thus ignoring changes in the hydrodynamics of hydrofoils under the action of the near-free-surface effect. This paper studies and explores the hydrofoil motion in near-free surfaces through the RANS viscous flow numerical simulation method, combined with overset mesh and adaptive mesh technology. Three different forms of motion are studied respectively, including a stationary fixed, a single-degree-of-freedom pitch and a two-degree-of-freedom heaving-pitching coupled hydrofoil. The effects of varying the immersion depth d on the lift and thrust generated were analyzed. Results indicate noticeable differences in the free surface action among different motion forms. When the water depth is less than one chord length C, the lift and thrust of the three motion forms decreased rapidly decrease. When d/C=1~1.5, the static fixed hydrofoil lift and thrust gradually approach the deep-water state. When d/C>2, the pitching motion of a single degree of freedom also tends to be stable. The two-degree-of-freedom motion is d/C>3. This finding shows that the effect of the near-free surface is closely related to the vertical motion. The greater the vertical motion is, the more severe the effect.

1. Introduction

The existence of a free water surface has adverse effects on the hydrodynamic performance of underwater vehicles or propellers [1]. Compared with previous studies, the research on bionic flapping hydrofoils has focused on the deep-water navigation environment [2]. For example, the German FESTO company [3], the EvoLogics company and the Technical University of Berlin developed Aqua Ray in 2008. The RoMan-II robotic fish was developed by Zhou et al. [4], Chew et al. [5], Meng et al. [6,7], and Cao et al. [8] have developed robotic fish that mimic manta rays.

However, relatively few studies have investigated the movement behavior of some wings that flap close to the water surface. Initially, these studies were all based on the experiments with fixed hydrofoils. Grue et

* Corresponding author.
E-mail address: Zhangjianing@dlmu.edu.cn

http://dx.doi.org/10.21278/brod76108

Received 8 July 2024; Received in revised form 16 September 2024; Accepted 26 December 2024;
Available online 7 January 2025
ISSN 0007-215X; eISSN 1845-5859

al. [9], studied the propulsion force, vortex wake and power to maintain the motion of nonviscous near-free surface flapping wings. The free surface waves were calculated, and the theoretical results were compared with the experimental results. The performance of a hydrofoil sailing near a water surface was tested by Kaneko et al. [10]. The effects of the angle of attack, depth of immersion, inflow velocity and surface effect on the performance and flow characteristics of hydrofoils were studied. Chen [11] studied the movement of fixed hydrofoils and flapping hydrofoils in the near-free surface. Gradually, the study of underwater flapping wing motion began. Barannyk et al. [12] conducted an experimental study on a flexible plate with coupled heave and pitch motion simultaneously. By changing the Strouhal number, the effects of the submerged depth and chord on the propulsive efficiency and thrust were determined. Liu [13] studied the effect of shallow water effect on the performance of a flapping wing device, and compared the performance and environmental impact of the device under shallow water and deep-water conditions. With the continuous development of new technologies, the Particle Image Velocimetry (PIV) technology has also been applied to capture the hydrofoil flow field. Huera-Huarte [14] used the Digital Particle Image Velocimetry (DPIV) technology to study the flow field and hydrodynamic performance of a vertically oscillating hydrofoil near a free surface, and studied the influence of the submerged depth on the hydrofoil. With the wide application of numerical calculation methods, researchers have gradually begun to use CFD simulation methods to study the near-free surface effect of flapping wing motion. Ozdemir et al. [15] used the Iterative Boundary Element Method to predict the flow around the fully submerged 2D and 3D hydrofoils operating close to a free surface. Wang et al. [16] and Xie and Zhen [17] used the RANS method to calculate the hydrodynamic characteristics of a two-dimensional hydrofoil under near-surface. Shang and Nikolaos [18] obtained the hydrodynamic thrust and hydrodynamic power of the ocean current turbine under different sea conditions via numerical simulation. Attiya et al. [19] adopted the large eddy simulation method to quantitatively analyze the influence of the lift and drag coefficients of the aspect ratio of the finite plate under near the free surface. Wang [20] calculated the hydrodynamic performance of near-surface hydrofoil by potential flow and viscous flow method. Amini [21] used the RANS method to study a pitching hydrofoil under a near-free surface and compared the results with experimental data. Shang et al. [22] systematically studied and presented the influence of changes in the resistance coefficient and lift coefficient via CFD. Lopes et al. [23] explored the possibility of energy extraction from waves by flapping hydrofoils. Ni et al. [24], Ling et al. [25], and Guo et al. [26] studied the hydrodynamic performance of the hydrofoils under a near free surface based on the CFD method.

In summary, the near-free surface effect of hydrofoils has always been a focus of attention. In many experiments, special attention has been given to the influence of free surfaces, and corresponding immersion depth requirements have been proposed. For flapping wing underwater robots, multicondition operations are becoming more common, and near-free surface operations are essential. Therefore, studying the near-free surface motion of flapping wings is highly meaningful. This study is conducted to meet the operational requirements of a batoid-inspired underwater vehicle near the water surface. The two-dimensional situation of pectoral fin propulsion in batoids can be simplified as flapping motion. Three types of motion forms are considered: static fixed hydrofoil (SFH), single-degree-of-freedom pitching motion (1DOF), and coupled heaving-pitching motion (2DOF). The viscous flow CFD method, combined with overset and adaptive mesh technology, was used to investigate the hydrodynamic performance of flapping wings with changes in immersion depth [27]. The differences in deep immersion depths for different motion forms were summarized.

2. Theoretical Methods

2.1 Numerical model

In this study, the Reynolds-averaged Navier-Stokes(RANS) was used as a fluid model solver. The mass conservation continuity equation and the momentum conservation governing equation of incompressible fluid are as follows [28,29]:

$$\frac{\partial \rho}{\partial t} + \frac{\partial \rho u_i}{\partial x_i} = 0 \tag{1}$$

$$\frac{\partial \rho u_i}{\partial t}+\frac{\partial}{\partial x_j}(\rho u_i u_j)=-\frac{\partial p}{\partial x_i}+\mu\frac{\partial}{\partial x_j}(\frac{\partial u_i}{\partial x_j}+\frac{\partial u_j}{\partial x_i})+\frac{\partial \rho \tau_{ij}}{\partial x_j}+f_s \tag{2}$$

In the above two formulas, ρ, p, μ and f_s represent the fluid density, average pressure, dynamic viscosity, and source term, respectively. u_i and x_i (x_j) are the velocity vector and coordinate vector of the tensor representation in the Cartesian coordinate system, respectively. $\tau_{ij}=-\overline{u_i' u_j'}$ is the Reynolds stress term.

StarCCM+ was used as a fluid solver. The PISO algorithm was used to solve the governing equation. The second-order upwind momentum discrete scheme and the first-order time discrete scheme were adopted. The new Reynolds stress term $\partial \overline{u_i' u_j'}/\partial x_j$ is an unknown quantity [30]. To make the equations closed, new equations were added, therefore different turbulence models were introduced. For the selection of the turbulence model, the SST $k-\omega$ turbulence model was adopted because the Reynolds numbers were mostly in the $10^4 \sim 10^5$ order of magnitude. This model is a hybrid model that combines the advantages of the far field calculation of the standard $k-\varepsilon$ model with the advantages of the low-Reynolds-number near-wall calculation of the standard $k-\omega$ model and has greater practicality and reliability.

For CFD calculation, the moving grid methods was developed and matured. Among them, the overset mesh method is the most commonly used method. In this method, the flow field is usually divided into two parts: the background domain and the overset domain [31], Fig 1. The data are exchanged at the overset boundary via numerical interpolation to realize the numerical calculation with a moving boundary. Moreover, it has more advantages for the numerical simulation of large rigid body motion. In this work, this method was used to the movement of a rigid-flapping hydrofoil. The volume-of-fluid (VOF) method was applied in the numerical simulations to capture the free surface. For the *q* phase, its equation can be expressed as follows:

$$\frac{\partial f_q}{\partial t}+\frac{\partial u_i f_q}{\partial x_i}=0 \tag{3}$$

where $f_q=1$ indicates that the grid cell is entirely occupied by water, $f_q=0$ signifies that the grid cell is completely filled with air, when $0<f_q<1$ the grid cell represents the free surface.

In order to capture the free surface better, adaptive mesh refinement technique was introduced. Adaptive mesh refinement technology is a dynamic computing method that involves continuously monitoring mesh quality during the calculation and adjusting the mesh to meet adaptive criteria. This approach enhances both the accuracy and stability of the calculations [32].

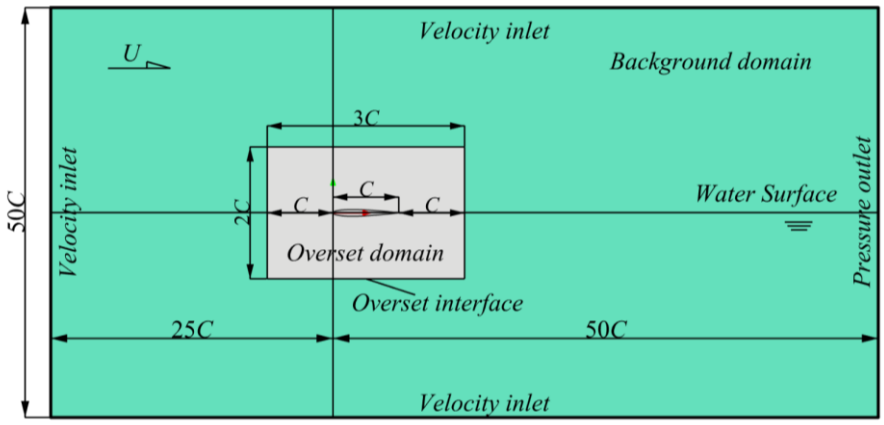

Fig 1. Background domain, overset domain and the boundary conditions

2.2 Hydrofoil motion equation

The propulsion process of the batfish underwater vehicle's pectoral fins is generally decomposed into spanwise and chordwise movements [33]. In the two-dimensional case, it is simplified into a sinusoidal motion with heave and pitch coupling. [34]. The equations of motion are defined as:

$$H(t) = h_{\max} \sin(\omega t) - d \tag{4}$$

$$\theta(t) = \theta_{\max} \sin(\omega t + \varphi) \tag{5}$$

where $H(t)$ and $\theta(t)$ represent the heave and pitch motion paths of foil over time, respectively. $h_{\max}$ and $\theta_{\max}$ represent the amplitudes of the heave and pitch, respectively. ω is the angular frequency, expressed as $\omega = 2\pi f$ and f is the frequency of motion, so $f = 1/T$. φ represents the phase difference between the two motions, which is set as $\varphi = -90^{\circ}$. In this work, the symmetrical hydrofoil NACA0012 was used as the research object. In Fig 2, the coupled motion process of a hydrofoil in a period at the immersion depth *d* can be clearly observed. θ_0 is the angle of the hydrofoil at the beginning of the calculation, which is equal to $-\theta_{\max}$.

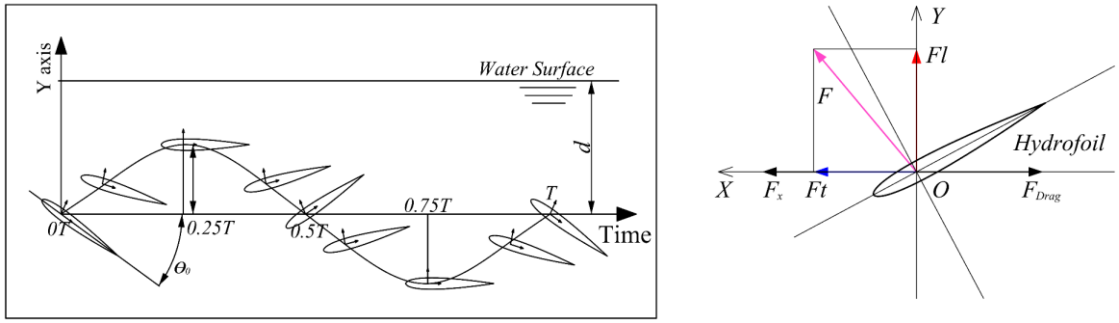

(a) flapping wing motion process (b) force decomposition

Fig 2. The hydrofoil coupling motion process in single period

In Fig 2(b), the thrust and lift forces are nondimensionalized as follows:

$$Ct = \frac{F_t}{\frac{1}{2}\rho U^2 CL}, \quad Cl = \frac{F_l}{\frac{1}{2}\rho U^2 CL}, \quad Cd = \frac{F_{Drag}}{\frac{1}{2}\rho U^2 CL} \tag{6}$$

where, the net thrust and lift coefficients are Ct and Cl ,respectively. Similarly, the drag coefficient can be expressed as *Cd*. The ρ , U and C are the fluid density, velocity and chord length, respectively. In the two-dimensional calculation, the span length L is 1. Note that the net thrust F_t , given by the thrust produced by the motion, F_x , minus the drag force F_{Drag} , i.e.:

$$F_t = F_x - F_{Drag} \tag{7}$$

3. Simulation

3.1 Numerical validation and convergence analysis

In view of the above theoretical methods, a practical case was used to prove the accuracy and feasibility of the numerical calculation method. The case described was the motion process of the NACA0012 hydrofoil with chord length *C*. Near the water surface, the tip of the pectoral fin emerges from the water. The chord length at the tip of a batoid's pectoral fin is relatively small and comparable to *C*=0.1m, which is the chord

length of our hydrofoil in this study. From a biomimetic perspective, a Reynolds number *Re* on the order of 10^4~10^5 is common for batoids [33].

Therefore, we chose to study the Reynolds number $Re = UC/\nu \approx 3\times10^4$. To verify the numerical scheme, we verified the work of Schouveiler et al. [35] and Ding [36]. Schouveiler studied the relationship between the thrust and efficiency of hydrofoils under pitch–heave coupling motion conditions with different Strouhal numbers ($St = 2h_{max}f/U$). Fig 3 shows the calculated results in this paper and Schouveiler's results. The numerical results are in good agreement with the experimental results. Compared with Ding's research, the single-degree-of-freedom pitching motion condition and the pitch-heave coupling motion condition of two degrees of freedom were set, respectively. The incoming flow speed was U=0.3m/s, the kinematic viscosity coefficient was $\nu = 0.1\times10^{-5}\ \mathrm{m^2/s}$. The movement frequency was f=2Hz, θ_{max}=30°, θ_0=-30°, and φ=-90° in Eq. (5). In the two-degree-of-freedom coupled motion, the amplitude of heave motion in Eq. (4) was set $h_{max}=C$ on the basis of the above parameter setting.

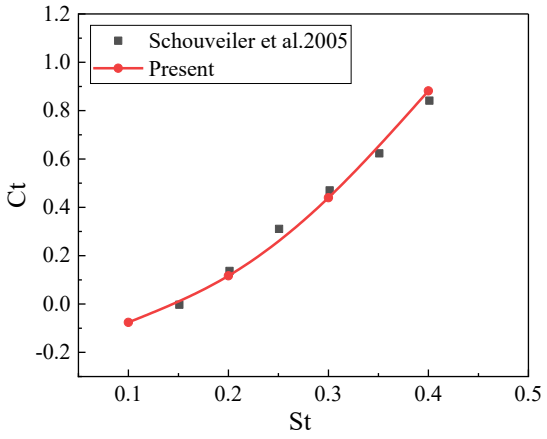

Fig 3. Comparison of the thrust coefficient and lift coefficient under the pitch-heave coupling motion conditions

When performing the calculations, y^+=1 was used. The grid height of the first layer of the wall boundary layer was set to 0.001C according to the Reynolds number.

$$\delta y = \frac{2y^+\mu}{u_\tau\rho},\quad u_\tau = \sqrt{\frac{\tau_w}{\rho}},\quad \tau_w = \frac{1}{2}\rho U^2 C_f,\quad C_f = \left[2\log_{10}(Re) - 0.65\right]^{-2.3} \tag{8}$$

where, u_τ is the friction velocity; τ_w is the wall shear stress; C_f is the skin-friction coefficient.

The mesh of *x*-size was set to 0.005*C*. The total number of cells was 180233. The numerical simulation results are shown in Fig 4.

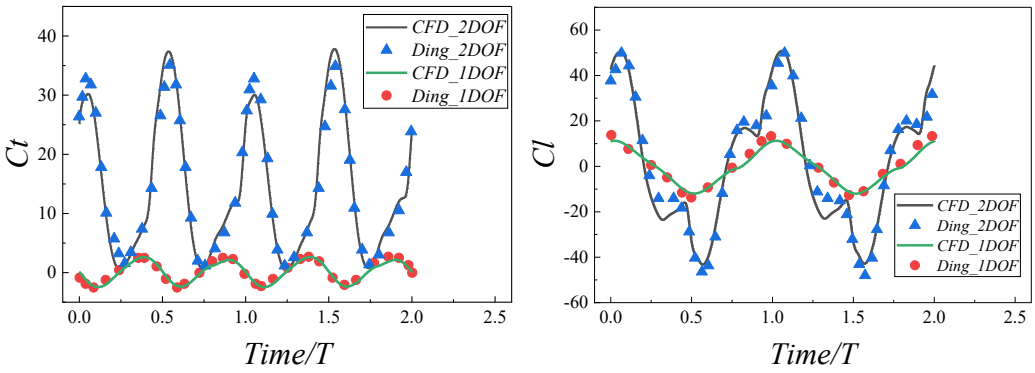

(a) Thrust coefficient *Ct* (b) Lift coefficient *Cl*

Fig 4. Comparison of thrust coefficient and lift coefficient under two working conditions

Fig 4 clearly shows that the calculated results in this paper are almost consistent with those in Ding's [36] work. Table 1 uses a 6-order Fourier series to regress the original data, and does performs correlation analysis on the CFD calculation results in this paper. Obviously, the calculated results are accurate. In two-degree-of-freedom coupled motion, because the flow field become complicated, there were errors at the peak, but the overall error was small. In general, the numerical calculation scheme in this paper is accurate and reliable.

Table 1. The CFD calculation results are compared with Ding by correlation coefficient

		Ding's	Present
1DOF	Cl	0.9998	0.9864
	Ct	0.9924	0.9739
2DOF	Cl	0.9988	0.983
	Ct	0.9965	0.9814

To avoid the influence of grid resolution and time step size on CFD simulation results, typically three sets of numerical simulation schemes are typically established on the basis of the grids number and time step size [22,31]. The results are referred to as coarse solution S_3, medial solution S_2, and fine solution S_1. If the grid resolution and time step size achieve converge, then

$$R = \frac{\varepsilon_{21}}{\varepsilon_{32}} = \frac{S_2 - S_1}{S_3 - S_2} \tag{9}$$

where, R denotes the convergence rate; generally, if $0 \le R \le 1$, it denotes convergence, $|R| > 1$ is divergence, and $-1 \le R < 0$ denotes oscillating convergence. ε_{21} and ε_{32} represent the differences between the coarse solution, the medial solution and the fine solution, respectively. In this work, the refinement ratio was selected $r_G = r_T = 1.5$:

$$r_G = \frac{N_{fine}}{N_{medial}} = \frac{N_{medial}}{N_{coarse}} = 1.5 \tag{10}$$

$$r_T = \frac{T_{fine}}{T_{medial}} = \frac{T_{medial}}{T_{coarse}} = 1.5 \tag{11}$$

where, r_G and r_T denote the mesh and time step refinement ratio, respectively; N_{fine} denotes the number of fine grid, and is followed by the solutions of the medial grid and the coarse grid. Similar pairs of time steps are T_{fine}, T_{medial}, and T_{coarse}.

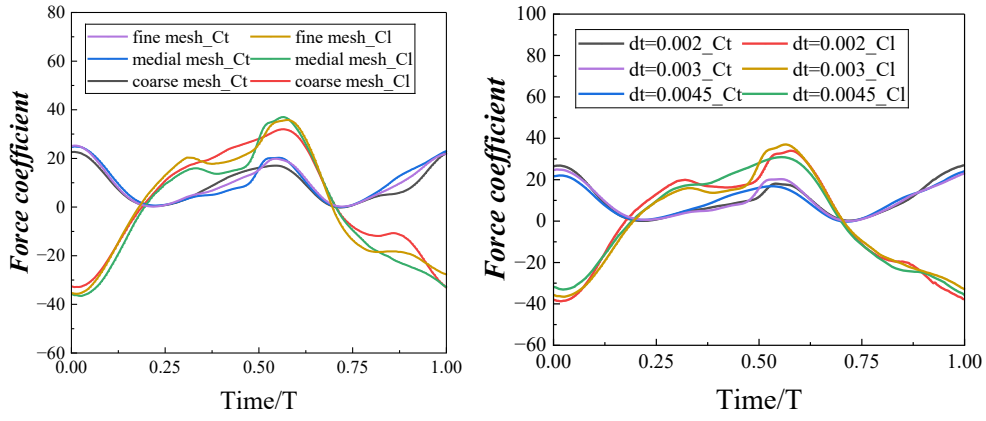

(a)2DOF mesh convergence (b)2DOF time step convergence.

Fig 5. Two-degree-of-freedom mesh and time step convergence analysis

The calculation cases were set according to the above CFD calculation grid and time step convergence method. The two-degree-of-freedom movement of the hydrofoil was verified when the working condition was d/c=1. After the flow field reached stability, the data of the adjacent four motion periods were taken, as shown in Fig 5. The calculated results of the six cases were very close. In the two-degree-of-freedom simulation, due to the complexity of the flow field, there was a significant difference in the peak value. Obviously, the medial solution S_2 and the fine solution S_1 are the same. However, there are apparent differences in the results of the coarse solution S_3, whether it is grid convergence or a time step. These two moments are the maximum vertical velocities of the hydrofoil, especially in the vicinity of the $0.5T$ and $1T$ moments.

Table 2. Grid and time step convergence calculation

Numerical scheme		Mesh convergence			Time step convergence		
		S1	S2	S3	S1	S2	S3
		Grids number			Time step		
		269350	180233	125155	0.002	0.003	0.0045
2DOF	$\overline{Cl}$	-1.122	-1.275	-1.008	1.836	-1.275	-1.182
	$\overline{Ct}$	9.942	9.930	10.106	9.838	9.930	8.960
		S2-S1	S3-S2	R_G	S2-S1	S3-S2	R_T
	$\overline{Cl}$	-0.154	-0.267	0.576	-0.094	-3.111	0.30
	$\overline{Ct}$	-0.012	-0.176	0.069	0.091	0.970	0.095

In summary, the grid has a greater influence on the simulation results. This occurred because there was a significant error when the mesh scheme was S_3. To calculate convergence, we calculated the corresponding convergence rate through a time average of the thrust and lift coefficients, $\overline{Ct}$ and $\overline{Cl}$, i.e.,

$$\overline{Ct}=\frac{1}{T}\int_{T}^{T+1} Ct\mathrm{d}t\,,\ \ \overline{Cl}=\frac{1}{T}\int_{T}^{T+1} Cl\mathrm{d}t \tag{12}$$

The results are shown in Table 2. Obviously, both the grid and the time step are convergent. This shows that the numerical simulation scheme proposed in this paper is effective.

4. Results and Discussion

4.1 Static fixed hydrofoil (SFH)

The influence of submerged depth on the hydrodynamic performance of rigid fixed hydrofoils was studied. Similarly, NACA0012 was selected as the research object. The calculation domain and spatial discretization were set in the above verification process, the incoming flow velocity was set as U=0.5 m/s, and the gravity was considered. First, the deep-water sailing state of the hydrofoil in single-phase flow was calculated, and the angle of attack (AOA) of the hydrofoil was changed to θ=-15°~15° with an interval of 2.5°. The calculation results are shown in Fig 6(a).

When traveling in deep water, we can clearly see that the change in lift and resistance was approximately symmetric with the AOA θ=0°, where the change in lift force had an origin symmetric form. When the AOA $|\theta|$<7.5°, the lift force had a linear change trend; when the AOA $|\theta|$>7.5°, the lift is reduction. According to the vortex field, when the AOA was greater than 10°, the leading and tail edge eddies were obvious. The water flow began to separate, which caused periodic oscillation of the vertical force of the hydrofoil. Therefore, the lift force began to weaken within this range of the AOA, as shown in Fig 7. In the calculation process, gravity was taken into account. Therefore, subtracting the gravitational force from the lift results in the net lift. This is consistent with the results from similar studies referenced in this paper [37].

Fig 6(b) show that when the depth d/C <0.5, the thrust and lift were much lower than those in deep water. When the depth d/C> 0.5, it can be seen that the rising resistance clearly increased rapidly. When the depth d/C > 1.5, the resistance decreased to a stable value. The free surface and dynamic pressure fields at depths d/C =0.4 and d/C=0.8 were taken, as shown in Fig 8. When the depth of immersion was shallow, the easy flow of the free surface caused the wave shape of the water surface to rise on both sides and became depressed in the middle. The high velocity of water flowing over the upper surface of the hydrofoil produced an obvious low-pressure area.

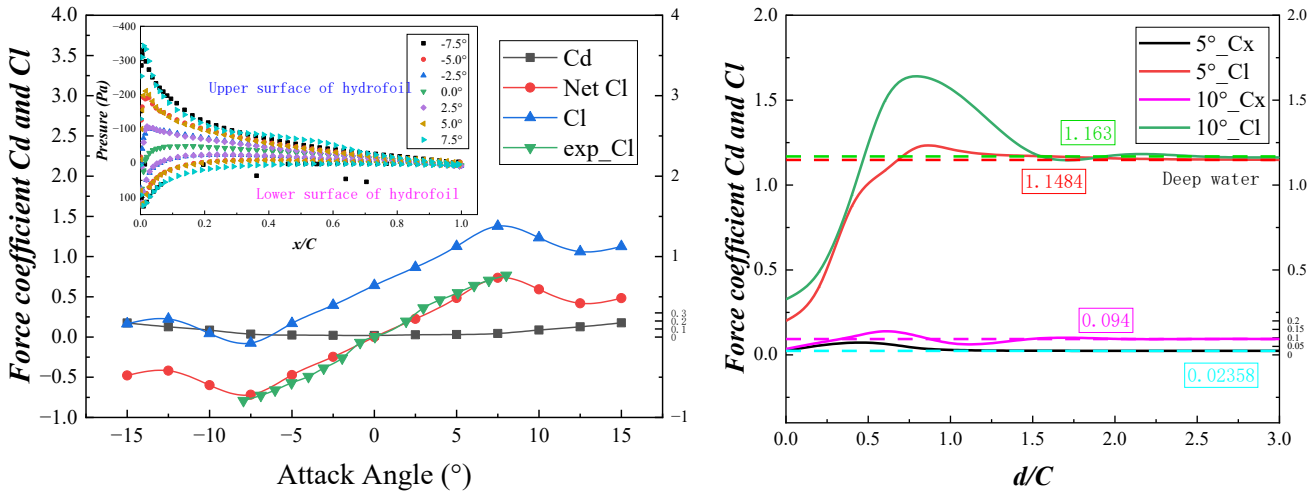

(a) Lift and drag coefficient (b)Lift and drag coefficient at different depths

Fig 6. Hydrodynamics of rigid stationary hydrofoil at different depths

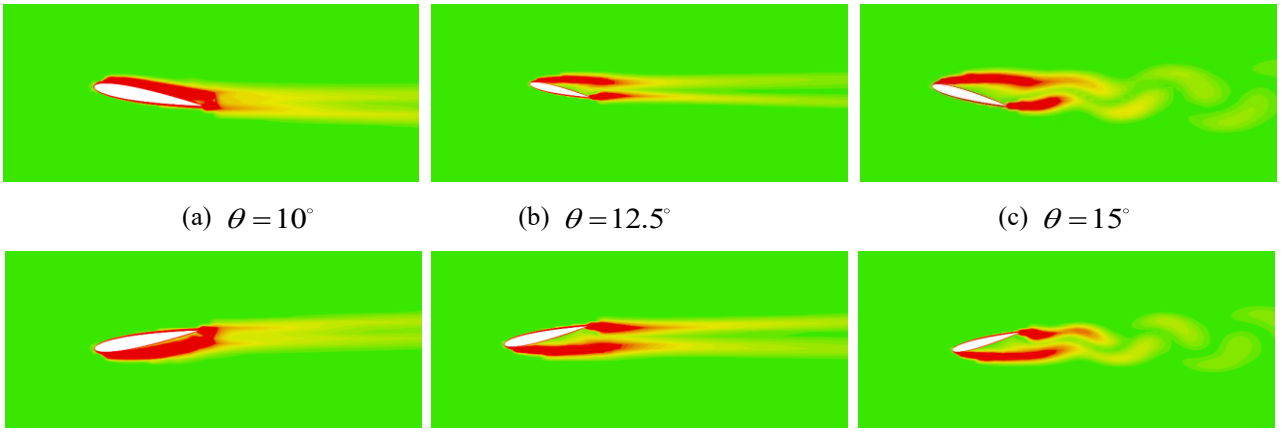

(a) $\theta = 10^{\circ}$ (b) $\theta = 12.5^{\circ}$ (c) $\theta = 15^{\circ}$

(d) $\theta = -10^{\circ}$ (e) $\theta = -12.5^{\circ}$ (f) $\theta = -15^{\circ}$

Fig 7. Vorticity field of hydrofoil at different attack angles

Fig 8(c) and (d) clearly shows that the lower surface of the hydrofoil was also in this low-pressure region; therefore, most of the upper and lower surfaces of the entire hydrofoil were in a state of negative pressure. Therefore, under shallow draft conditions, the hydrofoil easily caused the water flow to move along the surface, which leads to the loss of hydrodynamic performance [38]. As can be seen from the pressure distribution diagram in Fig 9, when the AOA of the hydrofoil increased at the same immersion depth, the leading edge pressure on the lower surface of the hydrofoil increased. Lift and resistance increase significantly at large AOA. The reason is that increasing the AOA increased the vertical projection area, which led to an increase in the lower surface pressure of the hydrofoil.

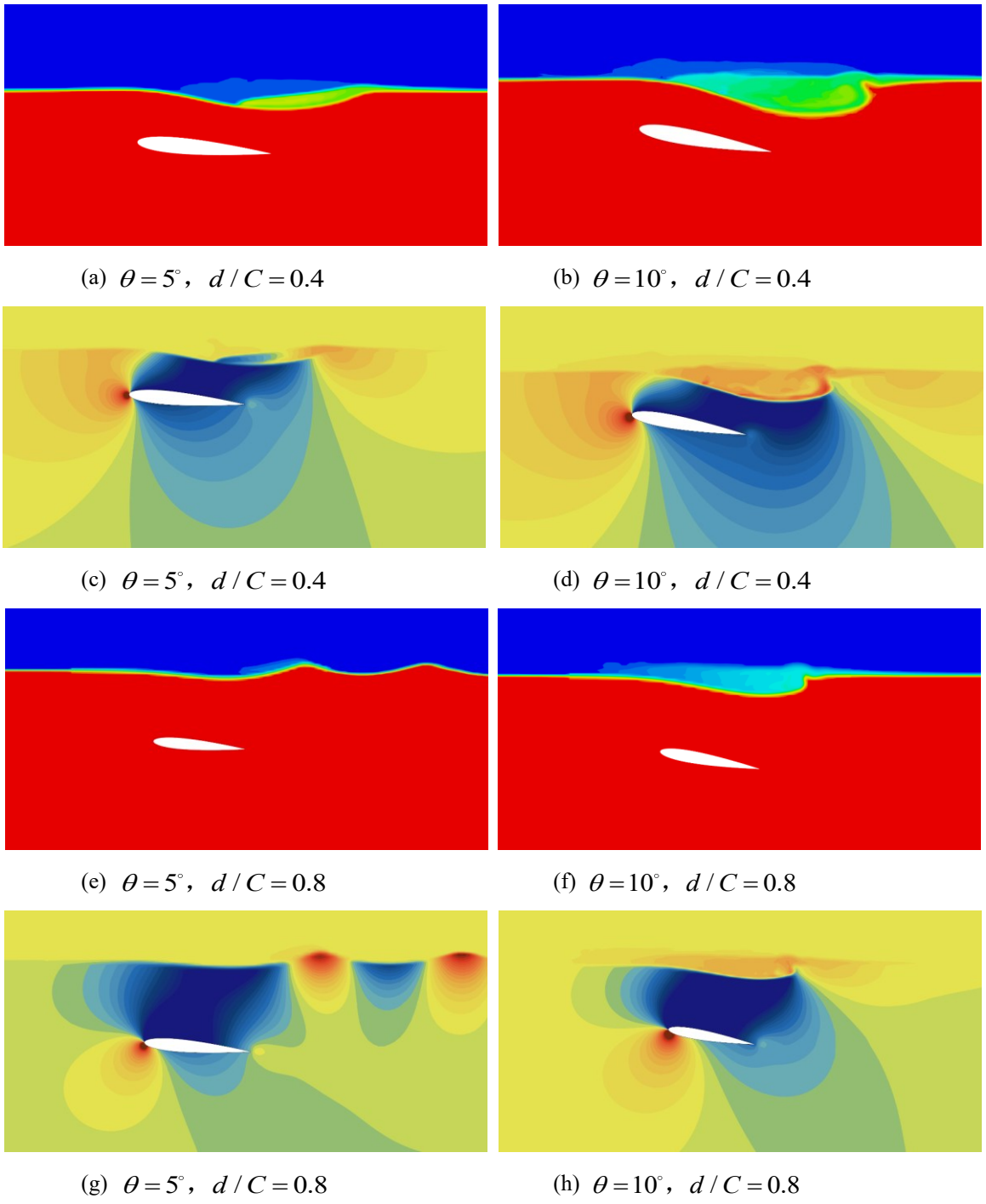

Fig 8. Free water surface and dynamic pressure field of hydrofoil at angles of attack of 5° and 10° and depths of *d/C*=0.4 and *d/C*=0.8

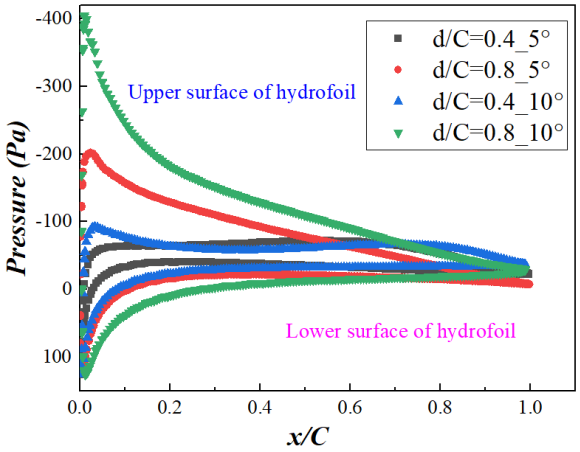

Fig 9. Dynamic pressure distribution of hydrofoil at angles of attack of 5° and 10° and depths of d/C=0.4 and d/C=0.8

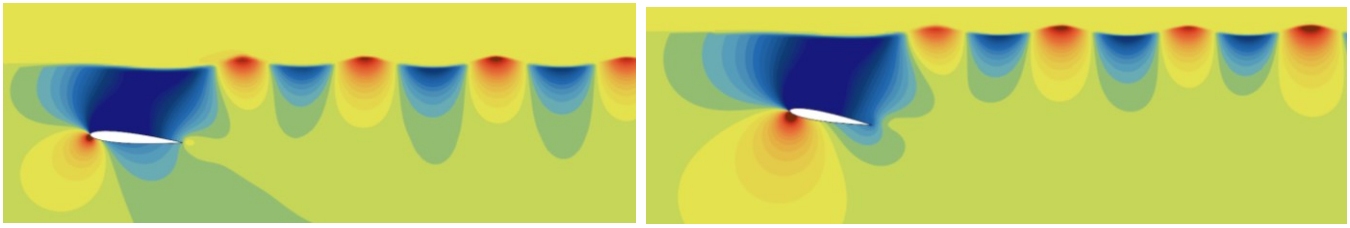

(a) d/C=0.8 , θ =5° (b) d/C=1, θ =10°

Fig 10. The velocity field of hydrofoil

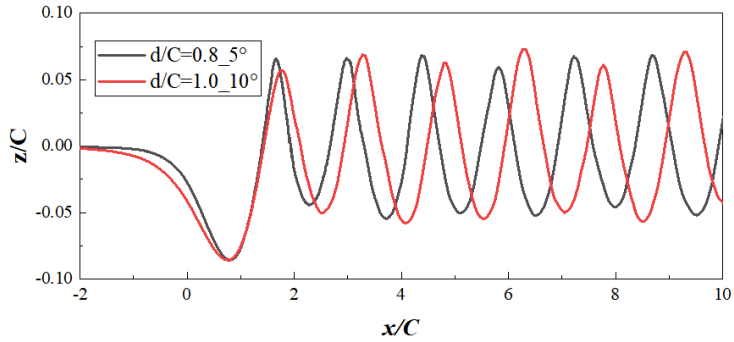

Fig 11. Free surface wave caused by hydrofoil

As the immersion depth increased, the obstructing effect decreased, and the lift and resistance gradually returned to the deep-water state. In this process, when the depth of immersion reached a certain position, the unsteady waves were generated at the tail of the hydrofoil, as shown in Fig 10 and Fig 11. The wave generated by the near-water surface effect was related to the depth of submersion and the AOA. The range of submergence depths that produce unsteady waves is about d/c=0.8 ~ 1, as shown in Fig 12 and Fig 13. At this point, the lift and drag are much greater than those in deep water. The indicates that the hydrofoil's lift-drag ratio will be enhanced within a specific depth of submersion [11,39].

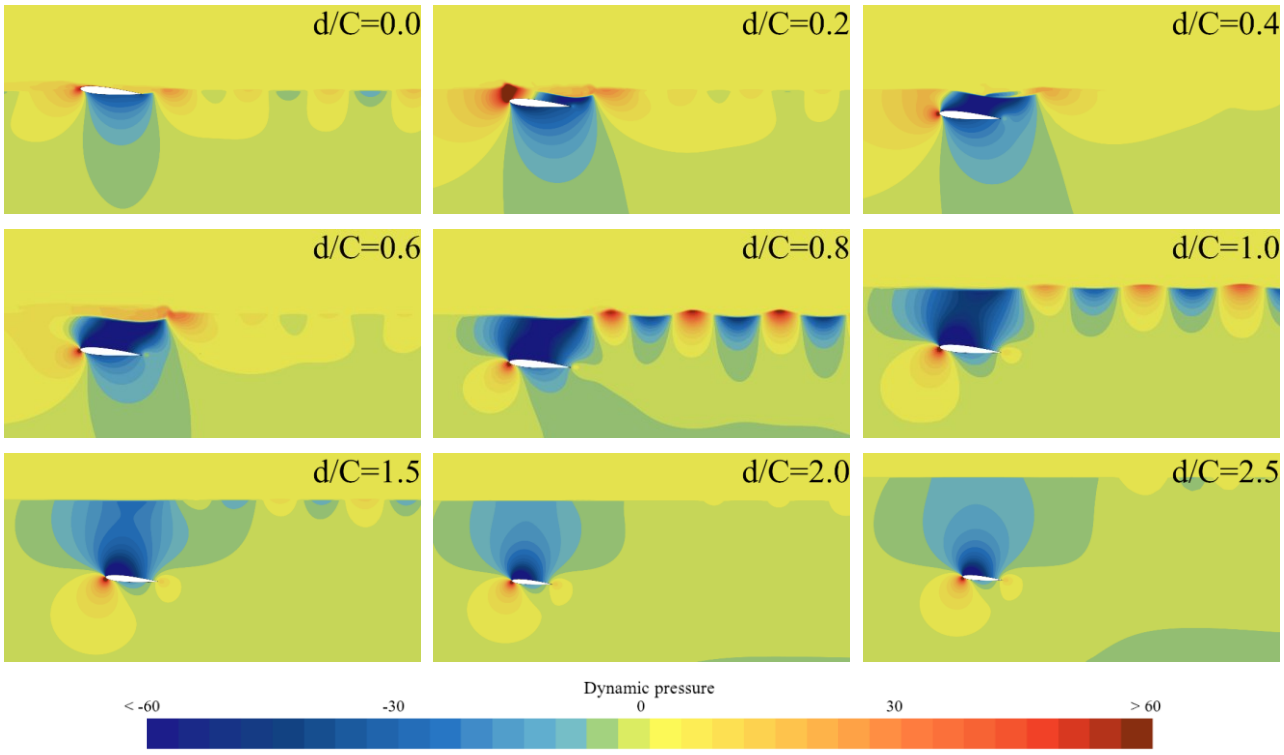

Fig 12. Hydrofoil dynamic pressure distribution at different immersion depths with attack angles of 5°

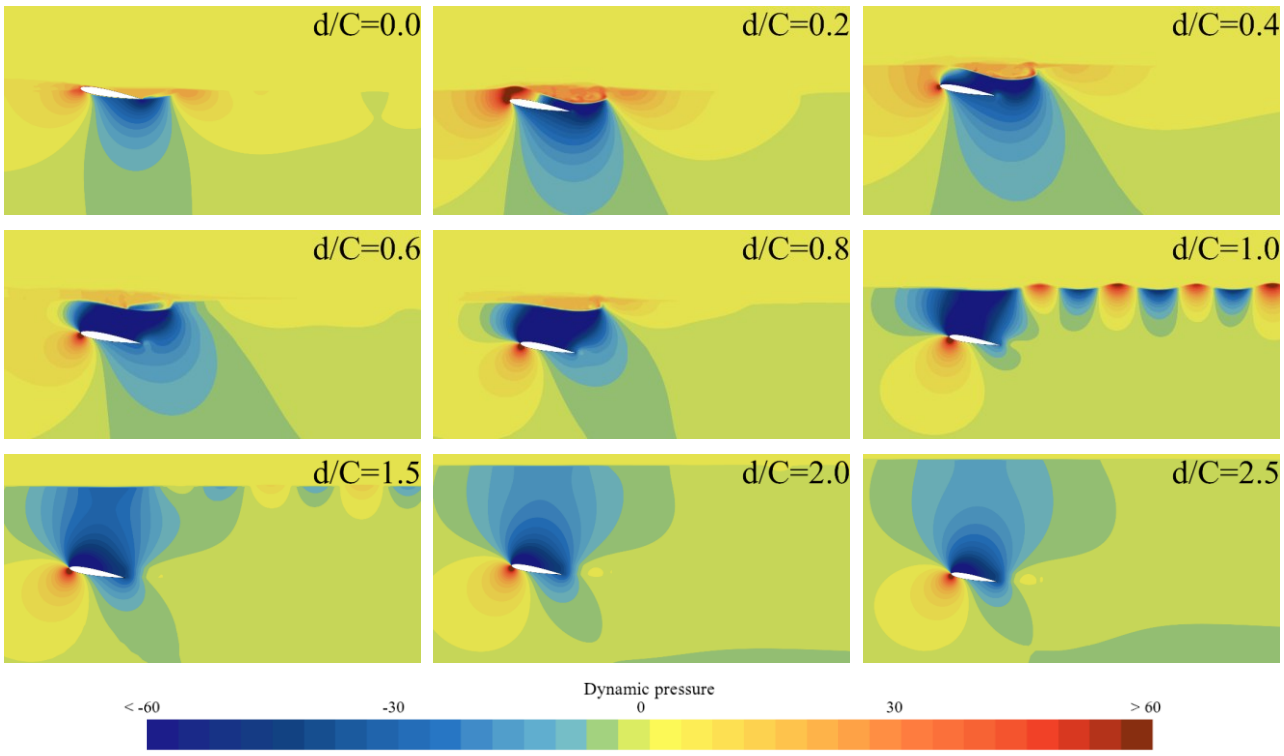

Fig 13. Hydrofoil dynamic pressure distribution at different immersion depths with attack angles of 10°

5. Single-degree-of-freedom pitching motion(1DOF)

Because the pitch motion is the main factor in generating thrust [40], the single-degree-of-freedom pitch motion with changing of submersion depth was studied. Several calculation conditions were set according to the chord length *C* of the hydrofoil. The calculation results are shown in Fig 14.

The time/T=0 in the figure indicates that the hydrofoil was in the midline position and flapping downward. When the depth was d/C=0~1, the lift force and thrust force clearly decreased with increasing immersion depth, especially at d/C<0.5. This impairment was particularly pronounced. As the depth increased, the thrust and lift were increased rapidly. Because the hydrofoil moves out of the water, the lift is almost zero.

To judge the degree of force decay, we integrated the force curve, that is, we described the impulse in a unit period. Then, there is

$$C_I = \frac{|F|t}{0.5\rho U^2 CLT} = \int_0^1 C_{force} \mathrm{d}\frac{t}{T} \tag{13}$$

where, C_I is the dimensionless coefficient of the impulse. The absolute value was designed to eliminate the negative sign effect. t represents time; C_{force} represents the lift or thrust force coefficient, and T represents the period of motion.

The thrust and lift impulse coefficient curves of the hydrofoil pitching motion in a single cycle are shown in Fig 15. The figure clearly shows that when the immersion depth was between d/C=0 ~ 1, the attenuation of the thrust and lift forces was pronounced and rapid, almost showing a linear attenuation. The maximum attenuation exceeded 65%. When the depth d/C> 0.8, the attenuation began to slow down and gradually approached the flat stage. When the depth d/C>2, it was basically flat, and the attenuation was only 1.45%.

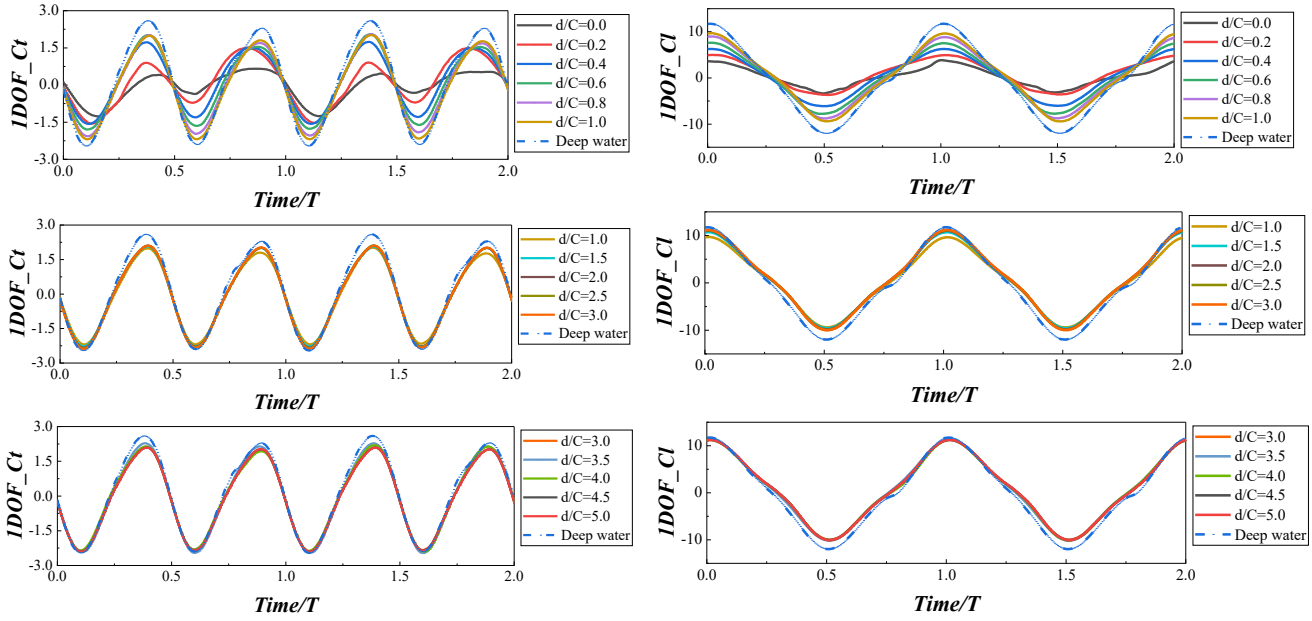

(a) Thrust coefficient Ct (b) Lift coefficient Cl

Fig 14. Thrust and lift coefficients of single-degree-of-freedom pitching motion affected by surface effects

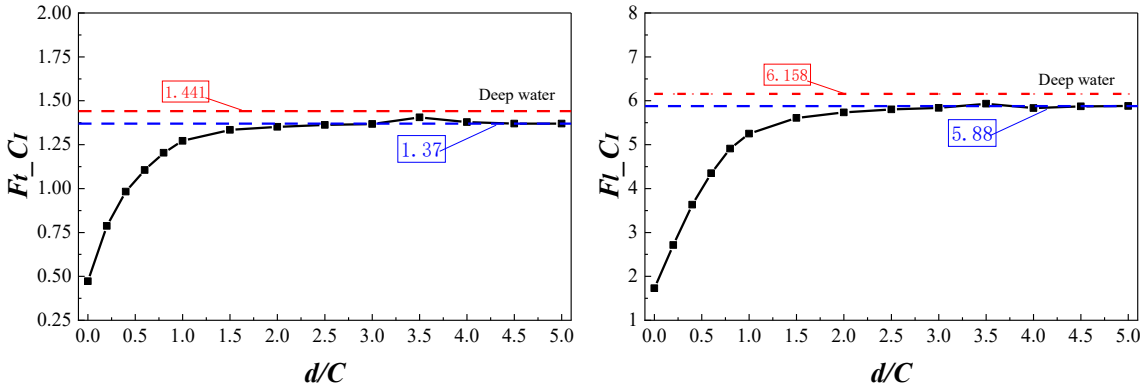

(a) Thrust impulse coefficient curve (b) Lift impulse coefficient curve

Fig 15. Thrust and lift impulse coefficient of near-surface hydrofoil pitching motion

5.1 Heaving-pitch coupling motion(2DOF)

To explore the influence of the rigid flapping wing motion under the free surface effect, the above 2DOF motion was taken as the research condition, and the near-surface flapping wing motion under different immersion depths d was specified. The motion parameters used were the same, and the depth range was set to d/C=0~5. Fig 16 shows the changes in the computed thrust coefficient Ct and lift coefficient Cl. The force changes still showed periodicity, which was similar to the movement in deep water. In Fig 16 , the starting position Time/T=0 essentially corresponds to the 0.5T shown in Fig 2; that is, the downstroke stage of the hydrofoil at the centerline. After 0.5T, the hydrofoil moved to the upstroke stage.

5.2 Thrust loss in 2DOF

As shown in Fig 16(a), when the depth was d/C=0~1, the thrust value increased with the increasing depth, and the difference between the two peaks during the movement was very obvious. In the first peak value, the increase of the value changing with depth was not as large as of the peak thrust value in the upsurge stage, that is, the increase of the second peak value was larger. When the hydrofoil left the water and moved through the air, the thrust quickly decreased to almost zero. Obviously, in the last 0.5T of the movement, the curve shape had a U shape. With the change in depth, the curve shape gradually changed into a V shape. This indicates that during the entire movement cycle, the hydrodynamic performance of the hydrofoil deteriorates after exiting the water. Moreover, the time when the peak appeared was different. The time when the first peak appeared was almost the same, and the average increase fluctuated between approximately 0.0048T, but when the second peak appeared was significantly delayed, and the average increase was approximately 0.0132T. The average difference between the first peak and deep water was -48.96%, and the second peak is -31.94%.

When the depth was d/C=1~3, the peak value gradually increased with increasing depth. When d/C=1~1.5, the first peak in motion rapidly increased to the deep-water peak. The second peak was still below deep water. When the hydrofoil moves out of the water at 0.4-0.46T, the thrust changes become chaotic. Thrust increased gradually at d/C=1.5~2.5. At d/C 2.5, the thrust change was almost the same as in deep water, only at the second peak, with a significant error, averaging -5.26%.

At depth of d/C=3~5, there is no doubt that the thrust change curve is almost recombined into a curve, and the height of the thrust change curve was similar to that of the deep-water flapping wing movement; similarly, there was a significant deviation only at the second peak.

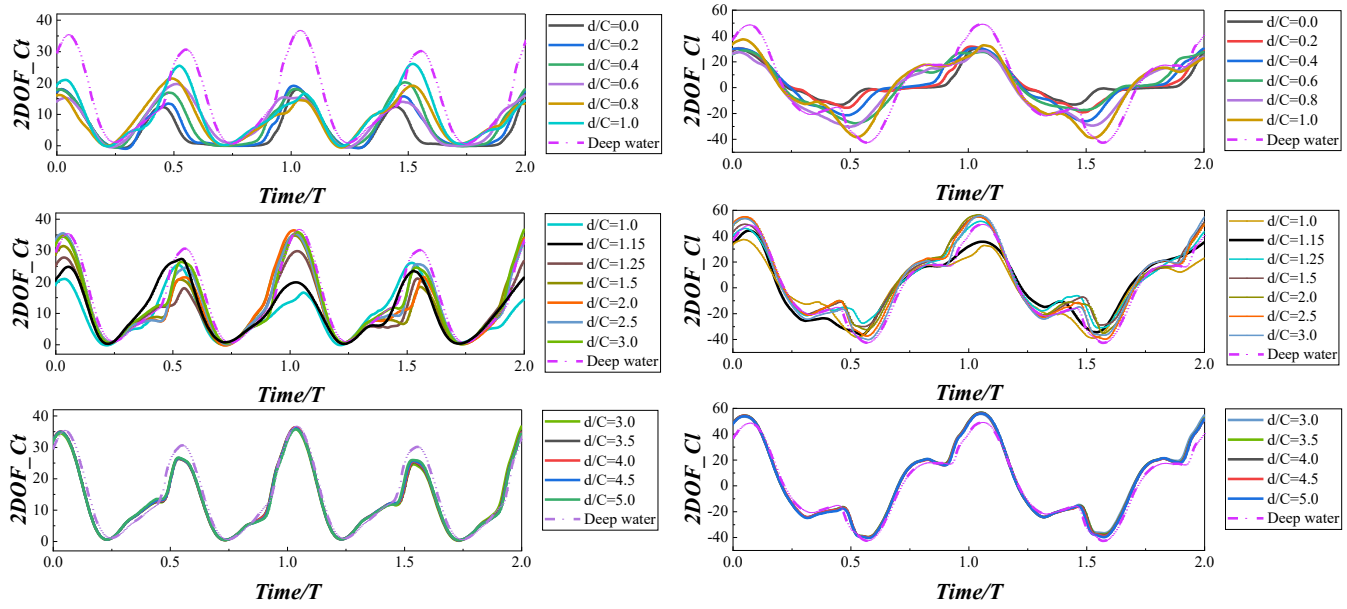

(a) Thrust coefficient Ct (b) Lift coefficient Cl

Fig 16. 2DOF thrust and lift coefficients affected by surface effects

Fig 17(a) shows the variation in the hydrofoil impulse coefficient with depth. When d/C>3, the impulse coefficient was 3.87% smaller than the impulse coefficient in deep water and tended to be stable. This shows that the thrust generated by the hydrofoil at this depth can be regarded as the deep-water motion state by ignoring the influence of the surface effect. The thrust loss was mainly at immersion depths of d/C=0~2, especially when d/C=0~1. The main cause of thrust loss was that the hydrofoil jumped out of the water surface to different degrees during the last 0.5T of movement, and the thrust was almost zero. The maximum thrust reduction was 63.7%.

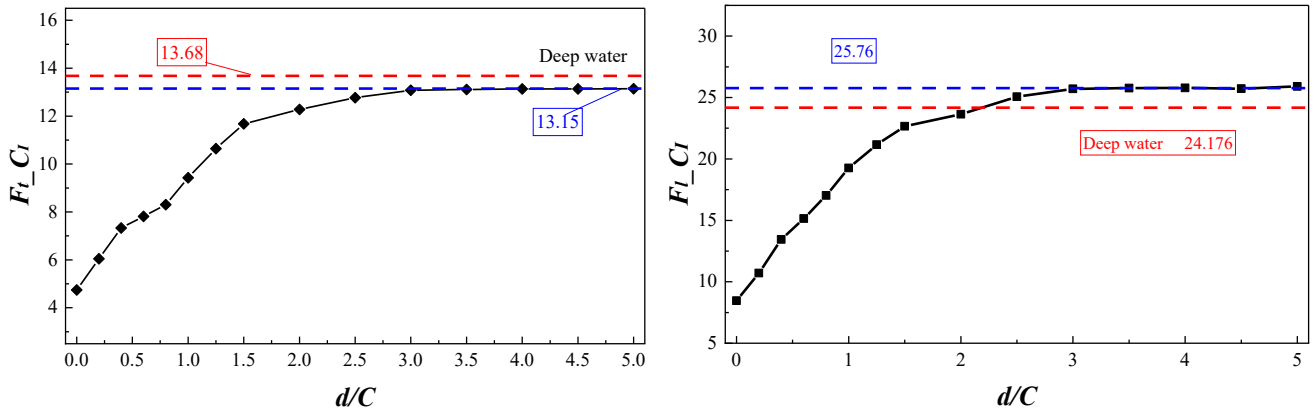

(a) Thrust impulse coefficient (b) Lift impulse coefficient.

Fig 17. The impulse coefficient varies with depth

5.3 Lift loss in 2DOF

The effect of immersion depth on the lift force was similar to that on the thrust force. Below, we elaborated the calculation results according to Fig 16(b). The down-stroke was significantly higher than the up-stroke. When Time/T=0~0.25, the increase in lift was not obvious. In contrast, when Time/T=0.5~0.75, the lift clearly increased with depth, and the peak lag phenomenon also occurred. When the water left the surface, the lift force was almost zero, and when the depth increased, the curve had the original change trend of change.

When the immersion depth d/C=0~3, the lift at the 0~0.5 T was close to the lift of deep-water navigation. At the 0.5~1T, the lift rapidly increased to the lift of deep-water movement. Then, it tended to flatten, especially when d/C >1.5 after, which the increase was slow. Overall, the variation in lift was similar to that in deep-water movement.

When the immersion depth d/C=3~5, the change in lift was basically synthesized into a curve, which was basically consistent with the change in lift during deep-water movement; only at the first peak value was greater than the original value, with a value of approximately 10.4%.

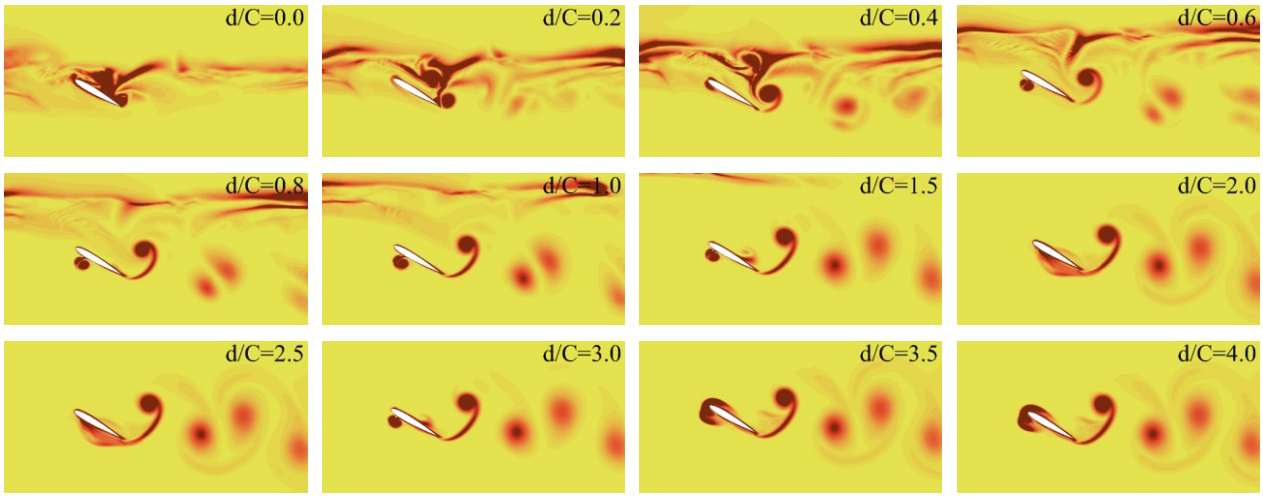

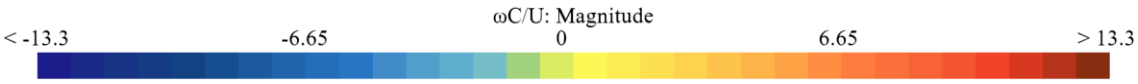

Fig 18. The vortex of single degree of freedom pitch motion under different immersion depth

The impulse coefficient of lift in a single period was calculated according to Eq. (13). In contrast to the thrust calculation, when the impulse coefficient of the lift force was calculated, to eliminate the influence of negative values on the calculation results, all lift forces were solved by taking absolute values, as shown in Fig 17(b). Obviously, when the depth was d/C=0~1, the attenuation of the lift changed almost linearly and only slowly increased to a stable state when d/C=1~3. Finally, when d/C>3, compared with the deep-water motion, the value was 6.5% greater, and the main error came from the deviation at the first peak.

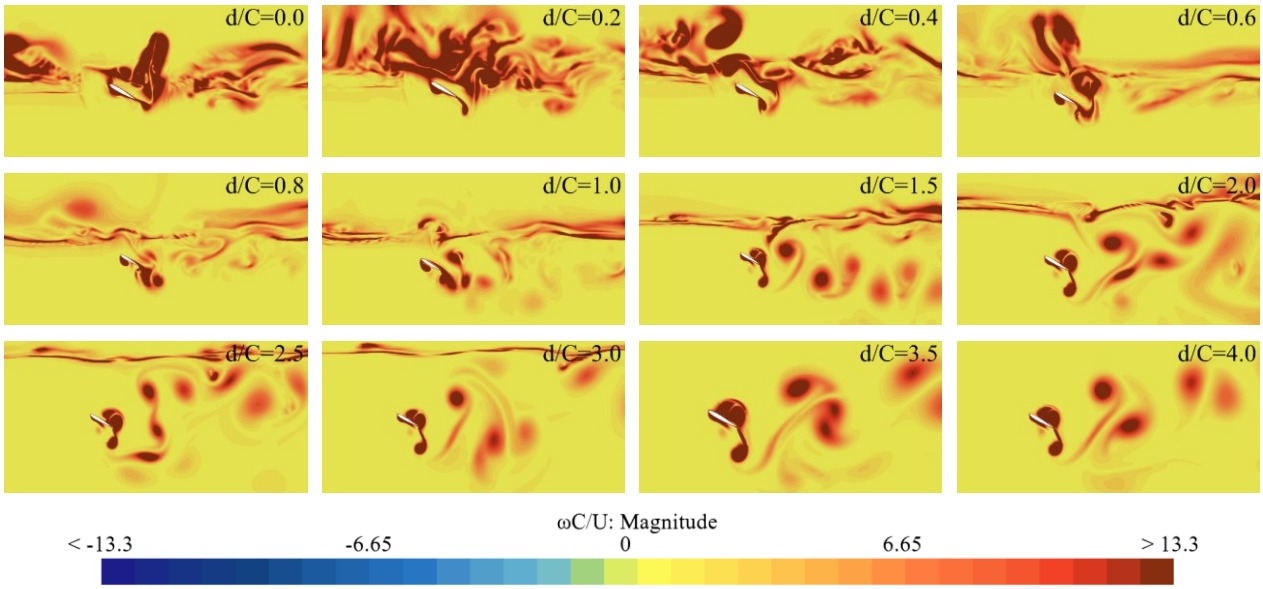

Fig 19. The vortex under different immersion depth with the coupled heave and pitch motion

5.4 Vorticity field

The special anti-Karman vortex produced by the movement of the flapping wing movement in water is the main feature, and we are very concerned about the interaction between the vortex and the hydrodynamic force [41,42,43].

Fig 18 and Fig 19 show the vortex field of the hydrofoil under different immersion depths. From the vortex distribution, it is obvious that the free surface has a great influence on the flapping wing movement. When the depth of immersion d/C<1, the flapping wing moved the water surface to produce waves and a complex vortex field. In the process of pitching near the water surface, the hydrofoil hit the water surface and was sucked into the air in the downstroke. The water splashed in the upstroke; thus, the energy was lost. With the increasing of water depth, the influence of the free water surface weakened and the eddy current field gradually returned to a stable state.

Unlike pitch motion of a single degree of freedom, the flapping wing movement of two degrees of freedom was more strongly affected by the free surface. The main reason is that the vertical motion was superimposed; therefore, the vortex field generated was much more complex. High-speed vertical motion led to severe splashing of the free surface, and there was no stable flow field to produce effective lift and thrust forces. When the immersion depth d/C>2, the lift and thrust began to stabilize.

6. Conclusion

In this work, a simplified 2D flapping wing for pectoral fin propulsion of manta ray underwater vehicle is studied, including three motion states of a rigid hydrofoil, namely, a stationary hydrofoil, a single-degree-

of freedom flapping wing and a two-degree-of-freedom flapping wing coupled with heave and pitch, are studied in a near-free-surface environment. After research and analysis, we reach the following conclusions:

(1) The lift and thrust loss of a stationary hydrofoil is caused by the wave generated on the free surface close to the hydrofoil during the movement, which results in a bulge at both ends of the water surface and a depression in the middle. The pressure field shows that the entire hydrofoil in the low-pressure area; therefore, the lift force of the hydrofoil is greatly reduced. It becomes stable when the submersion depth exceeds 1.5 times the chord length of the hydrofoil. However, before this depth, the lift and thrust of the hydrofoil increase sharply because of the near-water surface effect, which is significantly greater than the lift and thrust of the final stable layer in deep water. This is accompanied by noticeable wave generation.

(2) The lift and thrust generated by the hydrofoil with a single degree of freedom are also attenuated in the pitch motion. This attenuation is more than 60% greater than the lift resistance value in deep water. When the water depth $d/C>2$, it gradually stabilizes. For two-degree-of-freedom coupling flapping wing movement, the water depth $d/C>3$ can be stable. This finding indicates that the lift force and thrust force of the flapping wing motion are affected by the near-free surface and are related to the vertical motion. The greater the vertical motion is, the greater the water depth required for hydrodynamic stability.

(3) For the two-degree-of-freedom flapping wing movement near the water surface, although the motions of the upswing stage and the downswing stage are symmetrical, the hydrodynamic forces generated are not consistent. For the downstroke stage, the lift and thrust generated by the hydrofoil will rapidly increase to the values of the lift and thrust during deep-water movement. In the upstroke stage, when the hydrofoil movement is out of the water, the lift and thrust are clearly nearly zero, and the hydrodynamic curve shape is U shaped. As the water depth increases, it gradually becomes V shaped and consistent with deep-water movement.

Acknowledgement

This research was funded by the National Key Research and Development Program (2022YFC2805200); China COSCO Shipping Corporation Limited (Numerical and Experimental Technology Research of Ship Navigation Performance in High Sea States, 2023-2-Z001-02-01); the project funded by China Postdoctoral Science Foundation (2023M740466); the Natural Science Foundation of Liaoning Province (2024-MS-016); and the Fundamental Research Funds for the Central Universities (3132023123).

REFERENCES

[1] Chen, Q., Dong, X.Q., Yang, C.J, 2020. Vortex lattice method for the simulation of free-surface effects. *Chinese Journal of Hydrodynamics*, 35(03), 321-327.

[2] Cao, Y., Cao, Y. H., Huang, Q. G., Qu, Y. L., Pan G., 2023. A Review of the Underwater Bionic Flapping Wing Robots. *Digital ocean & underwater warfare*，6(4), 380-405.

[3] FESTO. Aqua ray [EB/OL]. 2023. https://www.festo.com/PDF_Flip/corp/Festo_Aqua_ray/en/files/assets/common/downloads/Festo_Aqua_ray_en.pdf.

[4] Zhou, C.L., LOW, K.H., 2010. Better endurance and load capacity: an improved design of manta ray robot (RoMan-II). *Journal of Bionic Engineering*, 7, S137-S144. https://doi.org/10.1016/S1672-6529(09)60227-4

[5] Chew, C.M., Lim, Q.Y., Yeo, K.S, 2015. Development of propulsion mechanism for Robot Manta Ray., *2015 IEEE International Conference on Robotics and Biomimetics (ROBIO)*, 6-9 December, Zhuhai, China, 1918-1923. https://doi.org/10.1109/ROBIO.2015.7419053

[6] Meng, Y., Wu, Z.X, Dong, H.J., Wang, J., Yu, J., 2022. Toward a novel robotic manta with unique pectoral fins. *IEEE Transactions on Systems, Man, and Cybernetics: Systems*, 52(3), 1663-1673. https://doi.org/10.1109/TSMC.2020.3034503

[7] Meng, Y., Wu, Z.X., Yu, J.Z., 2019. Mechatronic design of a novel robotic manta with pectoral fins. *2019 IEEE 9th Annual International Conference on CYBER Technology in Automation, Control, and Intelligent Systems (CYBER)*, 29 July-02 August, Suzhou, China, 439-444. https://doi.org/10.1109/CYBER46603.2019.9066722

[8] Cao, Y.H., Ma, S.M., Cao, Y.Z., Pan, G., Huang, Q.G., Cao, Y., 2022. Similarity evaluation rule and motion posture optimization for a manta ray robot. *Journal of Marine Science and Engineering*, 10(7), 908. https://doi.org/10.3390/jmse10070908

[9] Grue, J., Mo, A., Palm, E., 1988. Propulsion of a foil moving in water waves. *Journal of Fluid Mechanics*, 186, 393-417. https://doi.org/10.1017/S0022112088000205

[10] Kaneko, T., Uchida, M., Nishikawa, E., 2000. Performance of a hydrofoil travelling near a water surface. *Journal of the Kansai Society of Naval Architects*, 17-22.

[11] Chen, Q.R., 2011. Hydrodynamic investigation of three-dimensional oscillating hydrofoil near the free surface. *PhD thesis*, Huazhong University of Science and Technology, China.

[12] Barannyk, O., J. Buckham, B., Oshkai, P., 2012. On performance of an oscillating plate underwater propulsion system with variable chordwise flexibility at different depths of submergence. *Journal of Fluids and Structures*, 28, 152-166. https://doi.org/10.1016/j.jfluidstructs.2011.10.005

[13] Liu, W.D., 2017. A case study on tandem configured oscillating foils in shallow water. *Ocean Engineering*, 144, 351-361. https://doi.org/10.1016/j.oceaneng.2017.09.059

[14] Huera-Huarte, F.J., 2023. Pitching foil propulsion performance decays near the free surface. *Ocean Engineering*, 272, 113663. https://doi.org/10.1016/j.oceaneng.2023.113663

[15] Ozdemir, Y.H., Cosgun, T., Barlas, B., 2021. Wave field generated by finite-span hydrofoils operating beneath a free surface. *Brodogradnja*, 72(1), 145-167. https://doi.org/10.21278/brod72108

[16] Wang, Z.D., Zhu, R.Q., 2004. Hydrodynamic characteristics of 2-dimensional hydrofoil moving near to free-water surface. *Ship Engineering*, 2004(03), 12-15.

[17] Xie, Y., Zhen, Y., 2011. Hydrodynamic characteristics of 3-dimensional hydrofoil near to free-water surface at viscous flow. *Journal of Naval University of Engineering*, 23(02), 22-26+35.

[18] Shang, Y.C., Nikolaos I.X., 2017. Numerical analysis of hydrodynamic performance of FX-83-W hydrofoil current turbine. *ASME 2017 International Mechanical Engineering Congress and Exposition*, 3-9 November, Tampa, Florida, USA. https://doi.org/10.1115/IMECE2017-70995

[19] Attiya, B., Altimemy, M., Caspar, J., Daskiran, C., Liu, I., Oztekin, A., 2019. Large eddy simulations of multiphase flows past a finite plate near a free surface. *Ocean Engineering*, 188, 106342. https://doi.org/10.1016/j.oceaneng.2019.106342

[20] Wang, T.C., 2017. Research on the hydrodynamic characteristic of a oscillating foil near free surface. *PhD thesis*, Harbin Engineering University, China.

[21] Amini, Y., Kianmehr B., Emdad H., 2019. Dynamic stall simulation of a pitching hydrofoil near free surface by using the volume of fluid method. *Ocean Engineering*, 192, 106553. https://doi.org/10.1016/j.oceaneng.2019.106553

[22] Shang, Y., Horrillo, J.J., 2021. Numerical Simulation and Hydrodynamic Performance Predicting of 2 Two-Dimensional Hydrofoils in Tandem Configuration. *Journal of Marine Science and Engineering*, 9(5), 462. https://doi.org/10.3390/jmse9050462

[23] Lopes D.B.S., Vaz G., Falcão de Campos J.A.C., Sarmento A.J.N.A., 2023. Modelling of oscillating foil propulsors in waves. *Ocean Engineering*, 268, 113316. https://doi.org/10.1016/j.oceaneng.2022.113316

[24] Ni, Z., Dhanak, M., Su T.C., 2021. Performance of a hydrofoil operating close to a free surface over a range of angles of attack. *International Journal of Naval Architecture and Ocean Engineering*, 13, 1-11. https://doi.org/10.1016/j.ijnaoe.2020.11.002

[25] Ling, X., Leong, Z.Q., Duffy, J., 2023. Effects of length-to-diameter ratio on a near free surface underwater vehicle, *Applied Ocean Research*, 138,103657. https://doi.org/10.1016/j.apor.2023.103657

[26] Guo, J., Lin, Y., Wang, Y., Lin, P.W., Li, H.N., Huang, H.C, Chen, Y., 2023. Numerical research on hydrodynamic characteristics of the disk-shaped autonomous underwater vehicle near free surface, *Ocean Engineering*, 288(2), 116175. https://doi.org/10.1016/j.oceaneng.2023.116175

[27] Ma, Z.X., Ji, N., Zeng, Q., Deng, X.B., Shi, C, 2024. Influence of scale effect on flow field offset for ships in confined waters. *Brodogradnja*, 75(1), 1-22. https://doi.org/10.21278/brod75106

[28] Zhang, L., Zhang, J.N., Shang, Y.C., 2021. A practical direct URANS CFD approach for the speed loss and propulsion performance evaluation in short-crested irregular head waves, *Ocean Engineering*, 219, 108287. https://doi.org/10.1016/j.oceaneng.2020.108287

[29] Dogrul, A., 2022. Numerical prediction of scale effects on the propulsion performance of Joubert BB2 submarine, *Brodogradnja*, 73(2), 17-42. https://doi.org/10.21278/brod73202

[30] Wei, Y.H., Zhang, J.N., Guo, Z.Y., Zhang, Y., Shang, Y.C., Zhang, L., 2023. Research on added waves resistance in misalignment paralleling of two ships. *SPIE - The International Society for Optical Engineering*, Tangshan, China, 12756. https://doi.org/10.1117/12.2686114

[31] Mikulec, M., Piehl, H., 2023. Verification and validation of CFD simulations with full-scale ship speed/power trial data, *Brodogradnja*, 74(1), 41-62. https://doi.org/10.21278/brod74103

[32] Foucart C., Charous A., Lermusiaux, P., 2023. Deep reinforcement learning for adaptive mesh refinement, *Journal of Computational Physics*, 491, 112381. https://doi.org/10.1016/j.jcp.2023.112381

[33] Zhang, D, Huang, Q.G., Pan, G., Yang, L.M., Huang, W.X., 2022. Vortex dynamics and hydrodynamic performance enhancement mechanism in batoid fish oscillatory swimming. *Journal of Fluid Mechanics*. 930, A28. https://doi.org/10.1017/jfm.2021.917

[34] Farooq H., Ghommem M., Saif Ullah Khalid M., Akhtar I., 2022. Numerical investigation of hydrodynamic performance of flapping foils for energy harvesting, *Ocean Engineering*, 260, 112005. https://doi.org/10.1016/j.oceaneng.2022.112005

[35] Schouveiler, L., Hover, F.S., Triantafyllou, M.S., 2005. Performance of flapping foil propulsion, *Journal of Fluids and Structures*, 20(7), 949-959. https://doi.org/10.1016/j.jfluidstructs.2005.05.009

[36] Ding, H., 2014. Reaseach on propulsion and motion characteristics of biomimetic flapping foil unmanned underwater vehicle. *PhD thesis*, Northwestern Polytechnical University, China.

[37] Cleaver, D., Wang, Z.J., Gursul, I., 2010. Vortex Mode Bifurcation and Lift Force of a Plunging Airfoil at Low Reynolds Numbers. *48th AIAA Aerospace Sciences Meeting Including the New Horizons Forum and Aerospace Exposition*, 4-7 January, Orlando, Florida, USA. https://doi.org/10.2514/6.2010-390

[38] Bouscasse, B., Colagrossi, A., Marrone, S., Souto-Iglesias, A., 2017. SPH modelling of viscous flow past a circular cylinder interacting with a free surface, *Computers & Fluids*, 146, 190-212. https://doi.org/10.1016/j.compfluid.2017.01.011

[39] Duncan, J.H., 1983. The breaking and Non-breaking Wave Resistance of a Two-Dimensional Hydrofoil. *Journal of Fluid Mechanics*, 126, 507-520. https://doi.org/10.1017/S0022112083000294

[40] Lu, Y., Cao, Y.H., Pan, G., Huang, Q.G., Dong, X., Cao, Y., 2022. Effect of cross-joints fin on the thrust performance of bionic pectoral fins. *Journal of Marine Science and Engineering*,10(7), 869. https://doi.org/10.3390/jmse10070869

[41] Triantafyllou, G.S., Triantafyllou, M.S., Grosenbaugh, M.A., 1993. Optimal thrust development in oscillating foils with applications to fish propulsion. *Journal of Fluids and Structures*, 7(2), 205-224. https://doi.org/10.1006/jfls.1993.1012

[42] Triantafyllou, M., Triantafyllou, G., Gopalkrishnan, R., 1991. Wake mechanics for thrust generation in oscillating foils. *Physics of Fluids A: Fluid Dynamics*. 3(12), 2835-2837. https://doi.org/10.1063/1.858173

[43] Read, D.A., Hover, F.S., Triantafyllou, M S., 2003. Forces on oscillating foils for propulsion and maneuvering. *Journal of Fluids and Structures*, 17(1), 163-183. https://doi.org/10.1016/S0889-9746(02)00115-9